

Active-Sensing Acousto-Ultrasound-based Rotorcraft Structural Health Monitoring via Adaptive Functional Series Models

Shabbir Ahmed

Ph.D. Candidate

Mechanical Engineering

Rensselaer Polytechnic Institute

Troy, NY, USA

Peiyuan Zhou

Ph.D. Student

Mechanical Engineering

Rensselaer Polytechnic Institute

Troy, NY, USA

Fotis Kopsaftopoulos

Assistant Professor

Aerospace Engineering

Rensselaer Polytechnic Institute

Troy, NY, USA

ABSTRACT

In this work, the experimental assessment of the damage diagnosis performance of a full-scale rotorcraft blade is performed via stochastic time-varying time series models in the context of active sensing acousto-ultrasound guided wave-based damage detection and identification scheme. Ultrasonic guided waves, that are dispersive in nature, are represented via functional series time-varying autoregressive (FS-TAR) models. Next, the estimated time-varying model parameters are employed within a statistical decision-making framework to tackle damage detection and identification under predetermined type I error probability levels. Damage detection and identification based on coefficients of projection (COP) as well as time-varying model parameters are shown. Both damage intersecting and non-intersecting paths are considered in a full-scale rotorcraft blade as well as in an aluminum plate in pitch-catch configuration for the complete experimental assessment. The detailed damage diagnosis results are presented and the method's robustness, effectiveness, and limitations are discussed.

INTRODUCTION

In order to increase the reliability, safety, sustainability, and performance of aircraft/rotorcraft systems while reducing their maintenance cost, it is pervasive to integrate Structural Health Monitoring (SHM) technologies which may effectively enable their efficient life-cycle monitoring, and management (Refs. 1,2). SHM systems utilize distributed, permanently installed sensors at certain structural regions and apply diagnostic algorithms to extract meaningful health information from the sensing data.

SHM methods, depending on the area covered, may be broadly classified as local (part of the structure is covered) or global (entire structure is monitored) methods. On the other hand, based on the type of excitation used, they are classified as active (external excitation is used) or passive (no external excitation is used) methods. Ultrasonic guided wave-based SHM, which can be classified as active sensing local methods, uses guided elastic waves for monitoring the structure. Guided waves or Lamb waves are stress waves that propagate through thin structures. They can travel long distances in the non-dissipative medium such as metals and can be used to monitor a large part of the structure for tiny damage, cracks, or surface defects such as corrosion. In addition, these waves can easily be generated or detected with the help of piezoelectric transducers. Figure 1 and Figure 2 show the mechanism of guided wave generation and detection within a thin structure.

Damage index-based damage diagnosis algorithms are widely used in the literature in the context of guided wave-based dam-

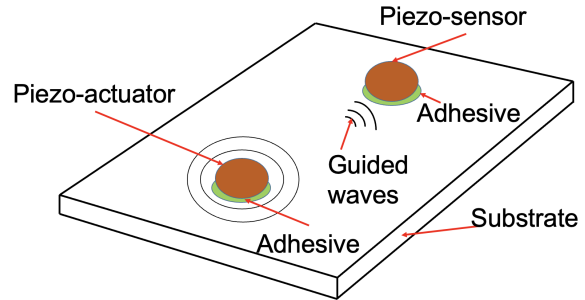


Fig. 1. Schematic diagram of the working principle of the acousto-ultrasound based SHM.

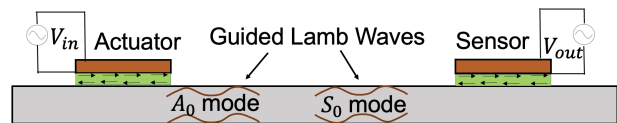


Fig. 2. Detailed side view of the substrate, adhesive and piezo sensors. Two modes of Lamb wave propagation, the symmetric (S_0) and antisymmetric (A_0), can be observed.

age diagnosis for their simplicity and ease of use. In this approach, features of the signal such as time of flight (ToF), amplitude or signal energy from an unknown structural state are compared to that of the healthy structure. In addition to time domain DIs, frequency domain or mixed time-frequency domain DIs were formulated to increase the sensitivity of the

damage detection process with the cost of reducing the robustness of the process (Refs. 3,4). Moreover, these DI-based approach are deterministic and do not account for the stochasticity inherent in the guided wave propagation signal (Ref. 5). Recently, steps have been taken towards formulating probabilistic DIs using Gaussian mixture models, Gaussian process regression or other statistical tools (Refs. 6–8). In the case of Gaussian mixture model, instead of comparing the individual DIs, their probability distributions are compared with the help of Kullback-Liebler (KL) divergence, or their modifications. However, these methods do not model the actual wave propagation for damage detection nor account for the underlying wave propagation dynamics.

In the context of vibration-based SHM methods, the use of stochastic time series models has shown great promise (Refs. 9, 10). Such models employ random excitation or response signals, statistical model building, and estimation techniques to represent the structural response. Moreover, statistical time series models possess unique advantages, such as no need for physics-based Finite Element (FE) or numerical models, no need for complete structural models, and inherent accounting of uncertainty as they are statistical in nature.

In this work, stochastic time-varying or adaptive time series models are introduced in the context of ultrasonic-guided wave-based SHM for active-sensing damage detection and identification. Unlike traditional vibration-based methods, guided-wave signals possess certain unique challenges, such as inherent non-stationary (time-varying) behavior and dispersion, limited signal length, complex effects due to reflections from boundary conditions, and high sensitivity to both environmental (temperature) and operating (loading) conditions (Refs. 11, 12). The main objective of this paper is the complete experimental assessment and evaluation of the proposed SHM scheme based on Functional Series Time-varying AutoRegressive (FS-TAR) (Refs. 13, 14) models on a full-scale rotorcraft blade for different damage sizes and locations. Damage has been simulated on different locations of the blade via the use of small added weights that introduces local elasticity changes in the blade. The rotorcraft blade used in this experiment is from an Airbus A350/H125 helicopter. It has a span of 4.7 m and a chord of 0.3 m. The weight of the blade is 31.15 kg. Before presenting the damage detection and identification results on this full-scale rotorcraft blade, damage diagnosis in an aluminum plate is discussed first as an initial experimental demonstration and assessment.

GUIDED WAVE SIGNAL REPRESENTATION

Guided waves are inherently non-stationary due to their time-dependent (evolutionary) characteristics. The time-varying nature of guided waves require the use of corresponding time-varying non-parametric and/or parametric models (Refs. 13, 15, 16). Stochastic parametric non-stationary (time-varying) models such as functional series time-dependent autoregressive moving average (FS-TARMA) models or related types and their extensions have been mainly used in the context of random vibration analysis (Refs. 13, 15, 16), with a detailed

review presented in (Ref. 13). In this study, the time-varying characteristics of the guided wave signals have been modeled via deterministic parameter evolution models, where the model parameters are deterministic functions of time. Functional series time-varying autoregressive (FS-TAR) models fall within this category.

Deterministic Parameter Evolution Models

Deterministic parameter evolution TAR representation imposes deterministic structure upon the time evolution of their parameters. This is achieved by postulating model parameters as deterministic functions of time, belonging to specific functional subspaces. Such representations are referred to as FS-TAR models. Their AR parameters, as well as innovations standard deviations, are all expanded within properly selected functional subspaces defined as

$$\mathcal{F}_{\text{AR}} \triangleq \{G_{b_a(1)}[t], G_{b_a(2)}[t] \dots G_{b_a(p_a)}[t]\} \quad (1)$$

$$\mathcal{F}_{\sigma_e} \triangleq \{G_{b_s(1)}[t], G_{b_s(2)}[t] \dots G_{b_s(p_s)}[t]\} \quad (2)$$

In these expressions, the “ \mathcal{F} ” designates the functional subspace of the indicating quantity and $G_j[t]$ a set of orthogonal basis functions selected from a suitable family (such as Chebyshev, Legendre, other polynomials, trigonometric or other functions). The AR and variance subspace dimensionalities are indicated as p_a and p_s , respectively, while, the indices $b_a(i)(i = 1, \dots, p_a)$ and $b_s(i)(i = 1, \dots, p_s)$ designate the specific basis functions of a particular family that are included in each subspace. The time-dependent AR and innovations standard deviation of an FS-TAR(na) _{$[p_a, p_s]$} representation may thus be expressed as

$$y[t] + \sum_{i=1}^{na} a_i[t] \cdot y[t-i] = e[t], \quad e[t] \sim \text{iid } \mathcal{N}(0, \sigma_e^2[t]) \quad (3)$$

$$a_i[t] \triangleq \sum_{j=1}^{p_a} a_{i,j} \cdot G_{b_a(j)}[t] \quad \sigma_e[t] \triangleq \sum_{j=1}^{p_s} s_j \cdot G_{b_s(j)}[t] \quad (4)$$

with $a_{i,j}$ and s_j designating the AR and innovations standard deviation coefficients of projection. An FS-TAR model is thus parametrized in terms of its coefficients of projection $a_{i,j}$ and s_j .

Coefficients of Projection Estimation

The problem of parameter estimation for deterministic parameter evolution TAR models, that is, FS-TAR models consists of determining the AR and innovations variance projection coefficient vectors ϑ and s , respectively.

$$\vartheta \triangleq [a_{1,1}, \dots, a_{1,p_a}; \dots; a_{na,1}, \dots, a_{na,p_a}]_{(na \cdot p_a) \times 1}^T \quad (5)$$

$$s \triangleq [s_1, s_2, \dots, s_{p_s}]_{p_s \times 1}^T \quad (6)$$

where ϑ represents the AR projection coefficient vectors.

with this notation the TAR model may compactly be written as:

$$A[\mathcal{B}, t, \vartheta] \cdot y[t] = e[t, \vartheta] \quad E\{e^2[t, \vartheta]\} = \sigma_e^2[t, \vartheta] \quad (7)$$

And the expanded form would be

$$y[t] + \sum_{i=1}^{na} \sum_{j=1}^{pa} a_{i,j} \cdot G_{b_a(j)}[t] \cdot y[t-i] = e[t, \vartheta] \quad (8)$$

By comparing Equation (7) and Equation (8), one can observe that

$$A[\mathcal{B}, t, \vartheta] = 1 + \sum_{i=1}^{na} \sum_{j=1}^{pa} a_{i,j} \cdot G_{b_a(j)}[t] \cdot \mathcal{B}^i \quad (9)$$

Equation (8) may also be written as:

$$y[t] = \phi_A^T[t] \cdot \vartheta + e[t, \vartheta] \quad (10)$$

with

$$\phi_A^T[t] \triangleq [-G_{b_a(1)}[t] \cdot y[t-1], \dots, b_a(pa)[t] \cdot y[t-na]]_{(na-pa) \times 1}^T \quad (11)$$

Estimation of the coefficients of projection vector ϑ may be based upon a prediction error criterion (PE) consisting of the sum of squares of the model's one-step-ahead prediction errors (residual sum of squares)

$$\hat{\vartheta} = \arg \min_{\vartheta} \sum_{t=1}^N e^2[t, \vartheta] \quad (12)$$

with $\arg \min$ designating minimizing the argument.

Since the residual $e[t, \vartheta]$ depends linearly upon the parameter vector ϑ , minimization of the PE criterion of Equation (12) leads to the ordinary least squares (OLS) estimator.

$$\hat{\vartheta}^{OLS} = \left(\frac{1}{N} \cdot \sum_{t=1}^N \phi_A[t] \cdot \phi_A^T[t] \right)^{-1} \cdot \left(\frac{1}{N} \cdot \sum_{t=1}^N \phi_A[t] \cdot y[t] \right) \quad (13)$$

The maximum likelihood (ML) estimation of the coefficients of projection vector ϑ may be obtained through the maximization of the log-likelihood function, which for the FS-TAR model and under the Gaussian assumption for the innovations sequence may be given as

$$\ln \mathcal{L}(\vartheta, \sigma_e | y^N) = -\frac{N}{2} \ln 2\pi - \frac{1}{2} \sum_{t=1}^N \left(\ln \sigma_e^2[t] + \frac{e^2[t, \vartheta]}{\sigma_e^2[t]} \right) \quad (14)$$

with $\sigma_e = [\sigma_e^2[1], \dots, \sigma_e^2[N]]^T$ constituting a nuisance parameter vector of high dimensionality while ϑ is a parameter vector

of low dimensionality. In such cases, the nuisance parameter vector may be profiled out from the log-likelihood function by considering the conditional maximum likelihood (CML) estimate of $\hat{\sigma}_e$ for known ϑ and substituting it into Equation (14). Towards this end,

$$\frac{\partial \ln \mathcal{L}}{\partial \sigma_e^2[t]} = 0 \implies -\frac{1}{2} \cdot \left[\frac{1}{\sigma_e^2[t]} - \frac{e^2[t, \vartheta]}{\sigma_e^4[t]} \right] \implies \hat{\sigma}_e^2[t] = e^2[t, \vartheta]$$

Then it follows that

$$\hat{\vartheta}^{ML} = \arg \max_{\vartheta} \{ \ln \mathcal{L}(\vartheta, \hat{\sigma}_e | y^N) \} = \arg \max_{\vartheta} \left[-\frac{1}{2} \sum_{t=1}^N \ln e^2[t, \vartheta] \right]$$

$\hat{\vartheta}$ is actually a pseudo-likelihood estimator which actually leads to the same point estimate with the original ML estimator of ϑ and σ_e . Once the FS-TAR coefficients of projection vector ϑ is estimated (which are constants), the time-varying parameter vector $\theta[t] = [a_1[t], a_2[t] \dots a_{na}[t]]_{na \times 1}$ can be estimated by multiplying with the basis functions as shown in Equation (4).

The associated covariance matrix for the estimated coefficient of projection vector ϑ can be obtained as (Ref. 14):

$$P_{\vartheta} = \frac{1}{N} \cdot \left\{ \frac{1}{N} \sum_{t=1}^N \frac{\phi_A[t] \cdot \phi_A^T[t]}{(g_s^T[t] \cdot \hat{s}^{ML})^2} \right\}^{-1} \cdot \left\{ \frac{1}{N} \sum_{t=1}^N \frac{\sigma_e^2[t] \cdot \phi_A[t] \cdot \phi_A^T[t]}{(g_s^T[t] \cdot \hat{s}^{ML})^4} \right\} \cdot \left\{ \frac{1}{N} \sum_{t=1}^N \frac{\phi_A[t] \cdot \phi_A^T[t]}{(g_s^T[t] \cdot \hat{s}^{ML})^2} \right\}^{-1} \quad (15)$$

Notice that the covariance matrix P_{ϑ} for the coefficients of projection vector ϑ is not time-varying. In order to perform time-varying damage detection and identification, time-varying parameters and the associated time-varying covariance matrix $P[t]$ would be necessary. The time-varying parameter vector $\theta[t] = [a_1[t] \ a_2[t] \ \dots \ a_{na}[t]]$ can be obtained via Equation (4). The associated time-varying covariance matrix can be obtained by following three steps: (i) sample m -times from a multivariate Gaussian distribution with mean ϑ and covariance P_{ϑ} ($\mathcal{N}(\vartheta, P_{\vartheta})$); (ii) obtain the associated time-varying parameters $\theta[t]$ from Equation (4) to obtain m -realizations of the parameters; (iii) estimate the sample mean $\theta[t]$ and covariance $P[t]$.

The estimation of the innovations standard deviation coefficients of projection may be achieved by the following procedure. An initial estimate of the estimated residual series $e[t, \hat{\vartheta}]$ variance is first obtained via a non-causal moving average filter (using a sliding time window) as follows:

$$\hat{\sigma}_e^2[t] = \frac{1}{2M+1} \sum_{\tau=t-M}^{t+M} e[\tau, \hat{\vartheta}] \quad (16)$$

with $2M + 1$ designating the window length. An initial estimate of the coefficients of projection vector s may then be obtained by fitting the obtained standard deviation $\widehat{\sigma}_e[t]$ to a selected functional subspace \mathcal{F}_{σ_e} . This leads to the overdetermined set of equations

$$\widehat{\sigma}_e[t] = \sum_{j=1}^{ps} s_j \cdot G_{b_s(j)}[t] = g^T[t] \cdot s \quad (17)$$

where

$$g[t] \triangleq [G_{b_s(1)}[t], G_{b_s(2)}[t], \dots, G_{b_s(ps)}[t]]_{ps \times 1}^T \quad (18)$$

This may be solved for the coefficients of projection s_j in a linear least squares sense.

The obtained initial estimate may subsequently be refined via maximum likelihood (ML) estimation. Accordingly, the refined estimator maximizes the loglikelihood of the residual standard deviation projection vector s given the residual series $e[t, \widehat{\vartheta}]$ (now treated as available measurements) with respect to the residual standard deviation projection vector s .

$$\widehat{s}^{ML} = \arg \min_s \left\{ -\frac{1}{2} \sum_{t=1}^N (\ln(g^T[t] \cdot s)^2) + \frac{e^2[t, \widehat{\vartheta}]}{(g^T[t] \cdot s)^2} \right\} \quad (19)$$

which is subject to the constraint $g^T[t] \cdot s > 0$. Estimation of s based upon this procedure constitutes a non-linear optimization problem, and is tackled via iterative optimization techniques that employ the previously obtained initial estimate as the starting point. An improved FS-TAR estimation may be achieved via the ML method, which maximizes the loglikelihood of the unknown vectors ϑ, s given the signal measurement y^N .

FS-TAR Model Structure Selection

Model structure selection of the FS-TAR model refers to the selection of the AR model order na , AR and innovations standard deviation functional subspaces $\mathcal{F}_{AR}, \mathcal{F}_{\sigma_e}$, respectively, their respective dimensionalities pa and ps , and their respective functional basis indices. Model structure selection could be based on either trial and error or integer optimization schemes, according to which models corresponding to various candidate structures are estimated, and the one providing the best fitness to the non-stationary signal is selected.

The fitness function may be the Gaussian log-likelihood function of each candidate model. The particular model that maximizes it is the most likely to be the actual underlying model responsible for the generation of the measured signal, in the sense that it maximizes the probability of having provided the measured signal values, and is thus selected. A problem with this approach is that the log-likelihood may be monotonically increasing with increasing model orders, and as a result, the overfitting of the measured signal occurs. For this reason, criteria such as the AIC (Akaike information criterion (Ref. 17))

or the BIC (Bayesian information criterion (Ref. 18)) are generally used and can be represented as follows:

$$AIC = -2 \cdot \ln \mathcal{L}(\mathcal{M}(\vartheta^N, (\sigma_e^2)^N) | x^N, y^N) + 2 \cdot d \quad (20)$$

$$BIC = -\ln \mathcal{L}(\mathcal{M}(\vartheta^N, (\sigma_e^2)^N) | x^N, y^N) + \frac{\ln N}{2} \cdot d \quad (21)$$

with \mathcal{L} designating the model likelihood, N the number of signal samples, and d the number of independently estimated model parameters. As it may be observed, both criteria consist of a superposition of the negative log-likelihood function and a term that penalizes the model order or structural complexity and thus discourages model overfitting. Accordingly, the model that minimizes the AIC or the BIC is selected. The Gaussian log-likelihood function of the model structure, $\mathcal{M}(\vartheta^N, (\sigma_e^2)^N) | x^N, y^N$, given the signal sample y^N and actuation x^N is given by:

$$\begin{aligned} \ln \mathcal{L}(\mathcal{M}(\vartheta^N, (\sigma_e^2)^N) | x^N, y^N) &= \ln f(\mathcal{M}(x^N, y^N | \vartheta^N, (\sigma_e^2)^N)) \\ &= \ln \prod_{t=1}^N f(e[t] | \vartheta^N, (\sigma_e^2)^N) \\ &= \sum_{t=1}^N \ln \left((2\pi\sigma_e^2[t])^{-\frac{1}{2}} \cdot \exp\left\{-\left(\frac{e^2[t]}{2\sigma_e^2[t]}\right)\right\} \right) \\ \ln \mathcal{L}(\mathcal{M}(\vartheta^N, (\sigma_e^2)^N) | x^N, y^N) &= \\ &- \frac{N}{2} \cdot \ln 2\pi - \frac{1}{2} \sum_{t=1}^N \left(\ln \sigma_e^2[t] + \frac{e^2[t]}{\sigma_e^2[t]} \right) \end{aligned} \quad (22)$$

As a result, the BIC equation can be written as:

$$BIC = -\frac{N}{2} \cdot \ln 2\pi - \frac{1}{2} \sum_{t=1}^N \left(\ln \sigma_e^2[t] + \frac{e^2[t]}{\sigma_e^2[t]} \right) + \frac{\ln N}{2} \cdot d \quad (23)$$

The innovations (one-step-ahead prediction error) variance $\sigma_e^2[t]$ may be estimated via Equation (16).

The ratio of the residual sum square versus the signal sum square (RSS/SSS) may also be used as another fitness criteria for the selection of the best model.

There are basically two search schemes for locating the best fitness model for FS-TAR case. One is known as an integer optimization scheme and another is known as a suboptimal search scheme. Irrespective of the particular scheme used, the basis function family (such as a given polynomial family, or a trigonometric family and so on) is assumed to be preselected. This preselection may be based on several factors such as prior knowledge or physical understanding of the system being investigated. It should be remembered that the selection of the basis functions family is more related to the parsimony of the representation rather than the accuracy. In fact, any family of basis functions may approximate any given curve with arbitrary accuracy, as long as a sufficient number of basis functions is used.

An *integer optimization scheme* consists of two distinct phases.

Phase I: Coarse Optimization: Phase I aims at determining promising subregions of the complete search space within which optimal model structures might be located. This is achieved via a genetic algorithm which maximizes the negative AIC or BIC. The algorithm incorporates: i) a non-linear ranking operator; ii) a stochastic universal sampling operator; iii) a two point cross-over operator; iv) a mutation operator; and v) a fitness based reinsertion operator.

Phase II: Fine Optimization: Phase II aims at refining the results of Phase I, and selecting the globally optimum structure. It operates in a neighborhood of each initial solution, and is based upon the concept of backward regression. It starts with the maximum values of the argument, and subsequently reduces either the model orders na or one of the subspace dimensionalities (pa, ps) until no further reduction in AIC or BIC is achieved. The procedure is repeated for all initial solutions, and the model structure corresponding to the globally optimum AIC or BIC is selected.

Although this scheme offers the possibility of more exhaustive searches, and is fully automated, it is exclusively based upon the fitness function (usually the AIC/BIC criteria), and may lead to overparameterizations which may affect the damage diagnosis accuracy.

The key characteristic of the *suboptimal search scheme* is the approximate decomposition of the structure selection problem into two subproblems: i) the model order na selection subproblem, and ii) the functional subspaces ($pa, ps, b_a(j), b_s(j)$) selection subproblem. In order to isolate the selection of the model orders from that of the functional subspaces, their interaction has to be minimized. This may be achieved by fixing one and optimizing for the others. To achieve optimum model order na , an extended (high dimensionality) and complete (all the consecutive functions up to the subspace dimensionality) functional subspaces are initially adopted and kept fixed for all model order na . With these fixed functional subspaces, the model order with the lowest AIC or BIC is selected.

In the second phase of the suboptimal search scheme, the selected model order na from the previous step is kept fixed, and the redundant functional subspaces are sequentially removed without significantly reducing model accuracy. This scheme is referred to as the suboptimal scheme as it may not provide the globally optimal model structure. However, from a practical stand point, this may be an effective approach due to its simpler implementation, low computational complexity, and flexibility in accounting for user provided structural information. Its main limitation is the use of an extended and complete functional subspaces which results in highly over-parameterized structure, and the estimation of the associated high number of coefficients of projection may pose statistical difficulties, that is, the number of available signal samples may be inadequate for this purpose.

Model Validation

Once a model has been obtained, it must be validated. Although this may be based on various criteria (depending on the model's intended use), formal validation procedures are typically based upon the posterior examination of the underlying assumptions, such as the model's residual series uncorrelatedness (whiteness) and Gaussianity. Due to the residual's time-dependent variance, the usual residual whiteness tests may not be applicable for non-stationary case. Yet, a relatively simple test, known as the residual sign test or runs test may be applied based on the number of sign changes in the series.

FS-TAR-BASED DAMAGE DIAGNOSIS

Coefficients of Projection Based Damage Diagnosis

Let $\hat{\vartheta}$ designate a proper estimator of the parameter vector ϑ . For a sufficiently long signal, the estimator is (under mild assumptions) Gaussian distributed with mean equal to its true value ϑ and a certain covariance P_ϑ , hence $\hat{\vartheta} \sim \mathcal{N}(\vartheta, P_\vartheta)$. Damage detection is based on testing for statistically significant changes in the parameter vector P_ϑ between the nominal state and current state of the structure through the hypothesis testing problem.

$$H_0 : \delta\vartheta = \vartheta_o - \vartheta_u = 0$$

null hypothesis–healthy structure

$$H_1 : \delta\vartheta = \vartheta_o - \vartheta_u \neq 0$$

alternative hypothesis – damaged structure

The difference between the two parameter vector estimators also follows Gaussian distribution, that is, $\delta\hat{\vartheta} = \hat{\vartheta}_o - \hat{\vartheta}_u \sim \mathcal{N}(\delta\vartheta, \delta P)$, with $\delta\vartheta = \vartheta_o - \vartheta_u$ and $\delta P = P_o + P_u$, where P_o, P_u designate the corresponding covariance matrices. Under the null (H_0) hypothesis $\delta\hat{\vartheta} = \hat{\vartheta}_o - \hat{\vartheta}_u \sim \mathcal{N}(0, 2P_o)$ and the quantity

$$Q = \delta\hat{\vartheta}^T \cdot \delta P^{-1} \cdot \delta\hat{\vartheta} \quad \text{with } \delta P = 2P_o \quad (24)$$

follows a χ^2 distribution with $d = \dim(\theta)$ (parameter vector dimensionality) degrees of freedom. As the covariance matrix P_o corresponding to the healthy structure is unavailable, its estimated version \hat{P}_o is used. Then the following test is constructed at the α (type I) risk level:

$$\begin{aligned} Q &\leq \chi_{1-\alpha}^2(d) \implies \\ H_0 &\text{ is accepted (healthy structure)} \\ \text{Else} &\implies \\ H_1 &\text{ is accepted (damaged structure)} \end{aligned}$$

where, $\chi_{1-\alpha}^2(d)$ designates the χ^2 distribution's $(1 - \alpha)$ critical points. As the covariance matrix P_o corresponding to the healthy structure is unavailable, its estimated version \hat{P}_o is used. It is to be noted here that, when \hat{P}_o is estimated from the data, the quantity Q in Equation 24 follows a Hotelling's

\mathcal{T}^2 distribution, which in turn, can be related to the Fisher's \mathcal{F} distribution. When $N \rightarrow \infty$, the \mathcal{F} distribution converges to χ^2 distribution. Damage identification may be based on a multiple hypothesis testing problem comparing the parameter vector ϑ_u belonging to the current state of the structure to those corresponding to different damage types $\hat{\vartheta}_A, \hat{\vartheta}_B, \dots$.

Time-Varying Damage Diagnosis

In this method, damage diagnosis of a structure is based on a time-dependent characteristic quantity $Q[t] = f(\theta[t])$, which is a function of the time-varying parameter vector $\theta[t]$ of the FS-TAR model. Let $\hat{\theta}[t]$ designate a proper estimator of the time-varying parameter vector $\theta[t]$. For a sufficiently long signal, the estimator is (under mild assumptions) Gaussian distributed with mean equal to its true value $\theta[t]$ and a certain covariance $P[t]$, hence $\hat{\theta}[t] \sim \mathcal{N}(\theta[t], P[t])$. Damage diagnosis is then based on testing for statistically significant changes in the time-varying parameter vector $\theta[t]$ for each time instant between the nominal and current state of the structure through the hypothesis testing problem.

$$H_0[t] : \delta\theta[t] = \theta_o[t] - \theta_u[t] = 0$$

null hypothesis—healthy structure

$$H_1[t] : \delta\theta[t] = \theta_o[t] - \theta_u[t] \neq 0$$

alternative hypothesis – damaged structure

The difference between the two parameter vector estimators also follows Gaussian distribution, that is, $\delta\hat{\theta}[t] = \hat{\theta}_o[t] - \hat{\theta}_u[t] \sim \mathcal{N}(\delta\hat{\theta}[t], \delta P[t])$, with $\delta\theta[t] = \theta_o[t] - \theta_u[t]$ and $\delta P[t] = P_o[t] + P_u[t]$, where $P_o[t], P_u[t]$ designate the corresponding time-varying covariance matrices. Under the null ($H_0[t]$) hypothesis $\delta\hat{\theta}[t] = \hat{\theta}_o[t] - \hat{\theta}_u[t] \sim \mathcal{N}(0, 2P_o[t])$ and the quantity

$$Q[t] = \delta\hat{\theta}[t]^T \cdot \delta P[t]^{-1} \cdot \delta\hat{\theta}[t], \quad \delta P[t] = 2P_o[t] \quad (25)$$

follows a χ^2 distribution with $d = \dim(\theta[t])$ (parameter vector dimensionality) degrees of freedom. As the time-varying covariance matrix $P_o[t]$ corresponding to the healthy structure is unavailable, its estimated version $\hat{P}_o[t]$ is used. Then the following test is constructed at the α (type I) risk level:

$$Q[t] \leq \chi_{1-\alpha}^2(d) \implies$$

$H_0[t]$ is accepted (healthy structure)

Else \implies

$H_1[t]$ is accepted (damaged structure)

where, $\chi_{1-\alpha}^2(d)$ designates the χ^2 distribution's $(1 - \alpha)$ critical points. Damage identification may be based on a multiple hypothesis testing problem comparing the parameter vector $\hat{\theta}_u[t]$ belonging to the current state of the structure to those corresponding to different damage types $\hat{\theta}_A[t], \hat{\theta}_B[t], \dots$.

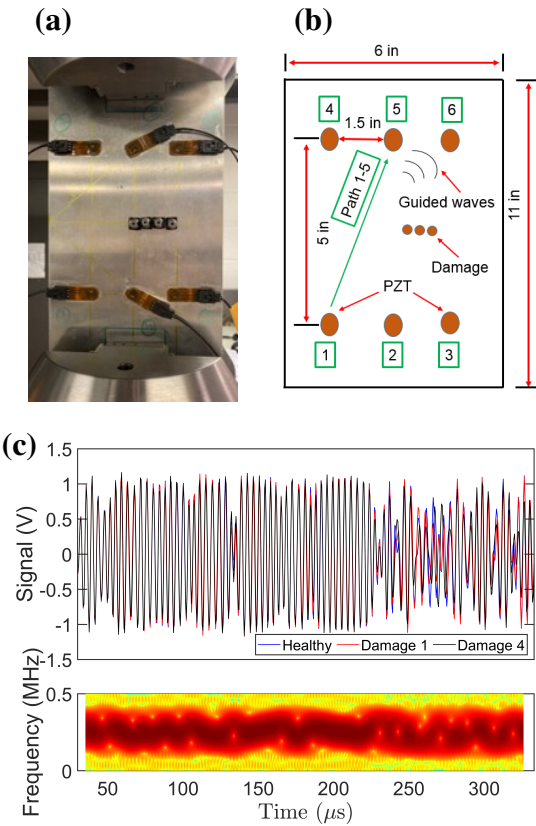


Fig. 3. (a) The aluminum plate used in this study; (b) a schematic of the plate's sensor layout and dimensions; (c) realization of the guided wave signal for healthy and damaged cases with a representative non-parametric spectrogram analysis.

TEST CASE I: ALUMINUM PLATE WITH SIMULATED DAMAGE

Experimental Setup and Data Acquisition for the Aluminum Plate

In this study, a 152.4×279.4 mm (6×11 in) 6061 aluminum coupon (2.36 mm/ 0.093 in thick) was used (Figure 3(a)). Using Hysol EA 9394 adhesive, six lead zirconate titanate (PZT) piezoelectric sensors (type PZT-5A, Acellent Technologies, Inc) of 6.35 mm ($1/4$ in) diameter and a thickness of 0.2 mm (0.0079 in) were attached to the plate and cured for 24 hours in room temperature. Figure 3(b) shows the dimensions of the plate, placement of the PZT transducers, and the path naming convention. Up to four three-gram weights were taped to the surface of the plate starting from its center-point to simulate local damage (Figure 3(b)).

Actuation signals in the form of 5-peak tone bursts (5-cycle Hamming-filtered sine wave, 90 V peak-to-peak, 250 kHz center frequency) were generated in a pitch-catch configuration over each sensor consecutively. Data were collected using a ScanGenie III data acquisition system (Acellent Technologies, Inc) from selected sensors during each actuation cycle at a sampling frequency of 24 MHz. Twenty signals from each sensor (wave propagation path) and damage state

were recorded. This led to a total of 100 data sets for each sensor. For the time-series modeling, the acquired signals were down-sampled to 2 MHz. This process resulted in 612-sample-long signals. Figure 3(c) presents indicative signal realization for different damage (health) state (top subplot) and non-parametric spectrogram of a single signal realization¹.

Parametric Identification and Damage Detection Results for the Aluminum Plate

In the context of the active sensing guided wave-based method, there are often multiple sensors installed at the area being monitored, and every actuator-sensor path in the network has to be examined in order to assess the integrity of the component. In the present study, Figure 3(b) shows the actuator-sensor layout, and six sensors/actuators have been used. Damage starts from the center of the plate and grows in magnitude to the right. In this study, simulated damages have been used in the form of weights mounted to the plate with tacky tapes. It has been shown that when the guided wave signal crosses the damage (known as the damage-intersecting path), a significant change can be observed in the signal with the increase in the damage size. On the other hand, for a damage non-intersecting path, one can observe that the received signals sustain significantly smaller change with the increase in damage size. Thus, information from the damage non-intersecting path naturally carries less information when it comes to damage detection and identification compared to damage-intersecting paths. In this case, path 3-4 has been chosen as representative damage intersecting path and path 2-4 as damage non-intersecting path.

Model selection of FS-TAR involves selecting the appropriate AR order na and the functional subspaces \mathcal{F}_{AR} and \mathcal{F}_{σ_e} . In the present case, the best FS-TAR model minimizes the BIC criteria utilizing an integer optimization scheme as described in (Refs. 13, 14). The integer optimization scheme utilizes coarse optimization based upon a genetic algorithm (population size 100, number of generations 100, crossover probability 0.8 and mutation probability 0.05) and fine optimization based upon the concept of backward regression. The functional subspaces considered are wavelet basis functions. For path 3-4, the best model occurred for $na = 4$ and the functional subspaces are $\mathcal{F}_{AR} = \{G_1[t], G_2[t], G_3[t], G_4[t]\}$ ($pa = 4$) and $\mathcal{F}_{\sigma_e} = \{G_1[t], G_2[t]\}$ ($ps = 2$). This is compactly written as FS-TAR(4)_[4,2]. Similarly, for path 2-4, the best model occurred for $na = 4$ and $\mathcal{F}_{AR} = \{G_1[t], G_2[t], G_3[t], G_4[t], G_5[t]\}$ ($pa = 5$) and $\mathcal{F}_{\sigma_e} = \{G_1[t], G_2[t], G_3[t]\}$ ($ps = 3$) compactly written as FS-TAR(4)_[5,3]. Maximum-likelihood estimator was used for estimating the coefficients of projection vector ϑ .

Figure 4 depict the first four AR coefficients of projection (COP) using the wavelet basis function for damage non-intersecting path 2-4 for all different structural states, namely: healthy, damage level 1, damage level 2, damage level 3,

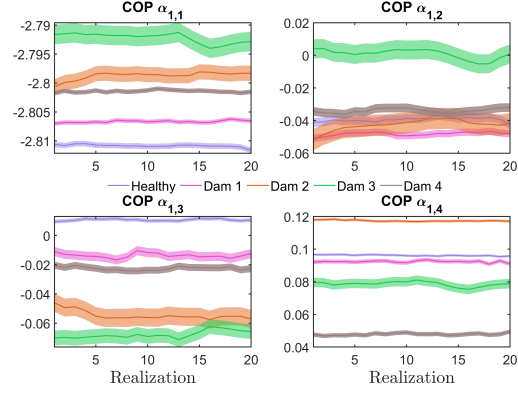


Fig. 4. Coefficients of projection (COP) for different structural states for the aluminum plate coupon for damage non-intersecting path 2-4 using the wavelet basis function: the COP mean is shown as solid lines and the associated ± 2 standard deviations as shaded regions.

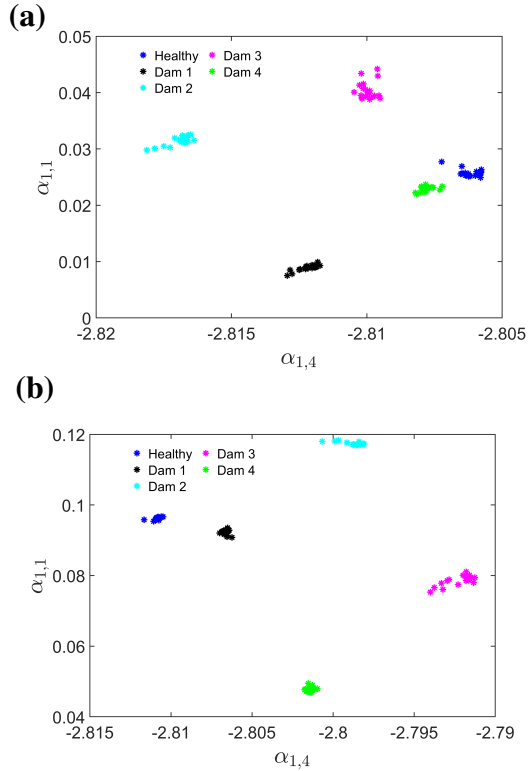


Fig. 5. Correlation between the coefficients of projection for different paths of the aluminum plate coupon: (a) for damage intersecting path 3-4; (b) for damage non-intersecting path 2-4.

and damage level 4. For wavelet basis functions and damage non-intersecting path 2-4, there are 20 AR COP in total ($na \cdot pa = 4 \cdot 5 = 20$). Among these 20 (16 for damage intersecting path 3-4) AR COPs, the first four, namely: $\alpha_{1,1}, \alpha_{1,2}, \alpha_{1,3}, \alpha_{1,4}$ are shown. For each state, 20 realizations are shown. The solid lines represent the mean COP values, and the shaded regions represent the ± 2 experimental standard deviation confidence intervals. In Figure 4 (for dam-

¹window length: 30 samples; 98% overlap; NFFT points: 30000 (zero-padding took place to obtain smooth magnitude estimates); frequency resolution $\Delta f = 666.66$ Hz.

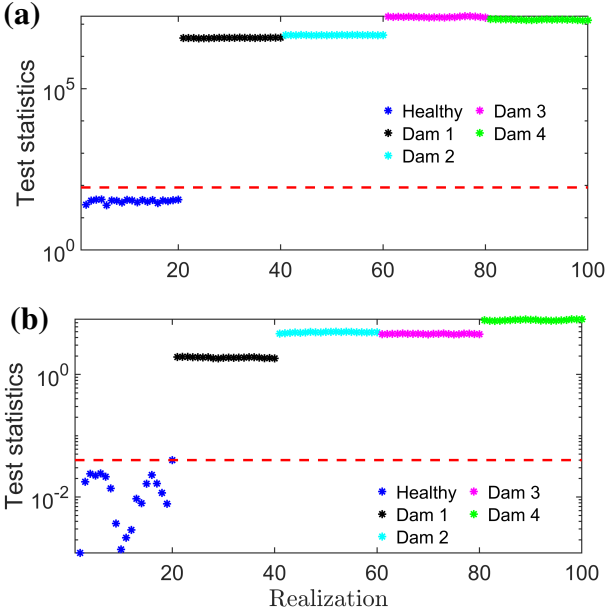


Fig. 6. Damage detection performance of the FS-TAR(4)[4,2] model for the aluminum plate for damage intersecting path 3-4: (a) using the experimental covariance matrix derived from 20 healthy realizations; and (b) using the FS-TAR(4)[4,2] model-based covariance matrix.

age non-intersecting path 2-4), for the COP $\alpha_{1,4}$, note that the COPs of different structural states are well separated and the confidence intervals are also narrower compared to the COP $\alpha_{1,1}, \alpha_{1,2}, \alpha_{1,3}$.

Figure 5(a) and (b) shows the correlation between the COP $\alpha_{1,1}$ and COP $\alpha_{1,4}$ for damage intersecting path 3-4 and damage non-intersecting path 2-4, respectively, using the wavelet basis function. Note that the COPs of different structural states are clustered together and well separated from each other both for damage intersecting path 3-4 and damage non-intersecting path 2-4. In general, when the COPs are clustered together, it is easier to perform damage detection and identification.

Figure 6 shows the damage detection performance of the damage intersecting path 3-4 using the wavelet basis functions. In Figure 6(a), the covariance matrix was derived from the 20 experimental healthy signals and in Figure 6(b), FS-TAR(4)[4,2] model-based covariance matrix was used. Note that for both cases, perfect damage detection was achieved. The α level used in Figure 6(a) was 1×10^{-12} . In Figure 6(b), it was manually adjusted as α level gets close to 1. Similarly, Figure 7 shows the damage detection performance of the damage non-intersecting path 2-4. Note that perfect damage detection was achieved in this case too. The α level used in Figure 7(a) was 1×10^{-12} while it was manually adjusted in Figure 7(b).

Figure 8 shows the damage identification performance for the damage non-intersecting path 2-4 for the wavelet basis function and using the experimental covariance matrix. Note that perfect damage identification was achieved with no missed classification. As for example, when identifying damage level

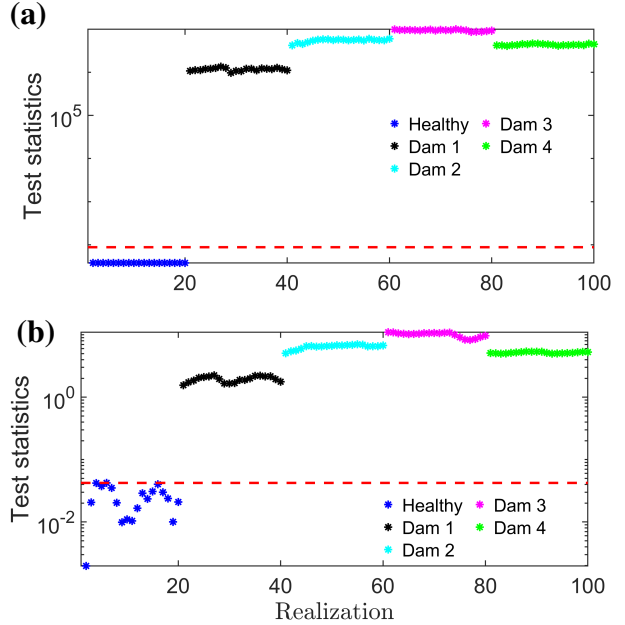


Fig. 7. Damage detection performance of the FS-TAR(4)[5,3] model for the aluminum plate for damage non-intersecting path 2-4: (a) using the experimental covariance matrix derived from 20 healthy realizations; and (b) using the FS-TAR(4)[5,3] model-based covariance matrix.

2 (Figure 8(b)), all the test statistics for damage level 2 remain below the threshold (dotted red line) and the test statistics for all other damage level go outside the threshold. Healthy test statistics are also shown to reinforce the fact that simultaneous damage detection and identification are possible using the same identified model structure.

Figure 9 shows the time-varying damage detection using the wavelet basis function for damage intersecting path 3-4. In Figure 9(a), experimental covariance matrix derived from 20 experimental healthy signals and in Figure 9(b), FS-TAR(4)[5,3] model-based covariance matrix were used. In this case, instead of using the constant COPs, four time-varying parameters (as the model order is $na = 4$) $\alpha_1, \alpha_2, \alpha_3$, and α_4 were used with the associated time-varying covariance. Note that the 20 healthy realizations of the time-varying test-statistics (solid blue lines) lie below the threshold (dotted red line) for all time instants. And the time-varying test statistics for damage level 1, 2, 3, and 4 (all realizations) crosses the threshold. As a result, perfect damage detection was achieved both for the experimental and theoretical covariance matrix used. Similarly, Figure 10 shows the time-varying damage detection using the wavelet basis function for damage non-intersecting path 2-4. Note that perfect damage detection was achieved in this case too. The α level used in Figure 9(a) and Figure 10(a) was 1×10^{-8} . On the other hand, it was manually adjusted for Figure 9(b) and Figure 10(b).

Figure 11 shows the time-varying damage identification performance for the aluminum plate for damage intersecting path 3-4. In this case, FS-TAR(4)[4,2] model-based covariance matrix was used. Note that perfect damage identification was

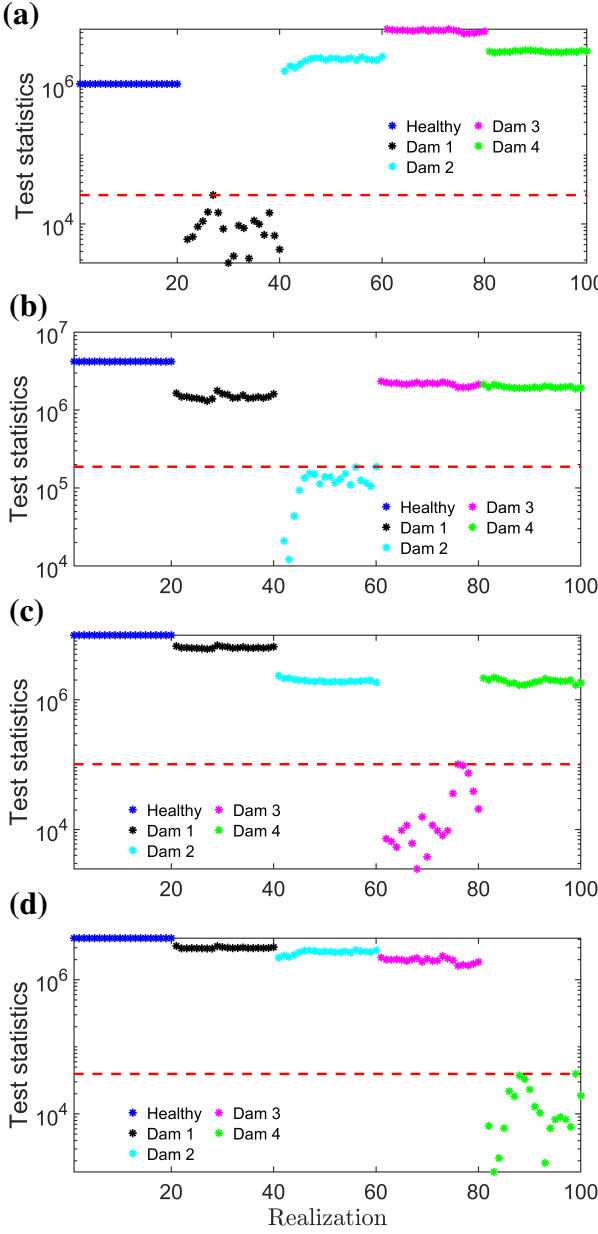


Fig. 8. Damage identification results of the FS-TAR(4)_[5,3] model for the aluminum plate for damage non-intersecting path 2-4 using the experimental covariance matrix derived from 20 healthy realizations: (a) damage level 1; (b) damage level 2; (c) damage level 3; (d) damage level 4.

achieved for all different damage levels.

TEST CASE II: HELICOPTER BLADE WITH SIMULATED DAMAGE

Experimental Setup and Data Acquisition for the Helicopter Blade

The second experimental setup consists of an Airbus H125 helicopter blade, which has a composite material construction. It has a span of 4.7 m and a chord of 0.3 m. The weight of the blade is 31.15 kg. The blade has its main spar made from wound roving glass fiber. A laminated woven glass fiber

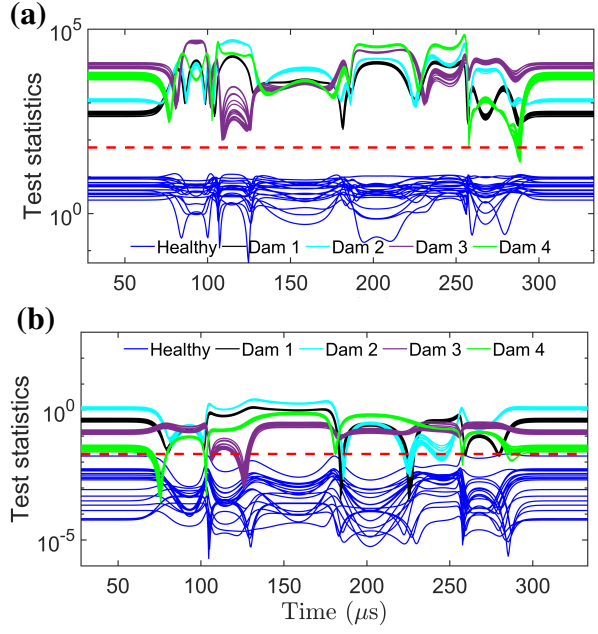


Fig. 9. Time-varying damage detection performance of the FS-TAR(4)_[4,2] model for the aluminum plate for damage intersecting path 3-4: (a) using the experimental covariance matrix derived from 20 healthy realizations; and (b) using the FS-TAR(4)_[4,2] model-based covariance matrix.

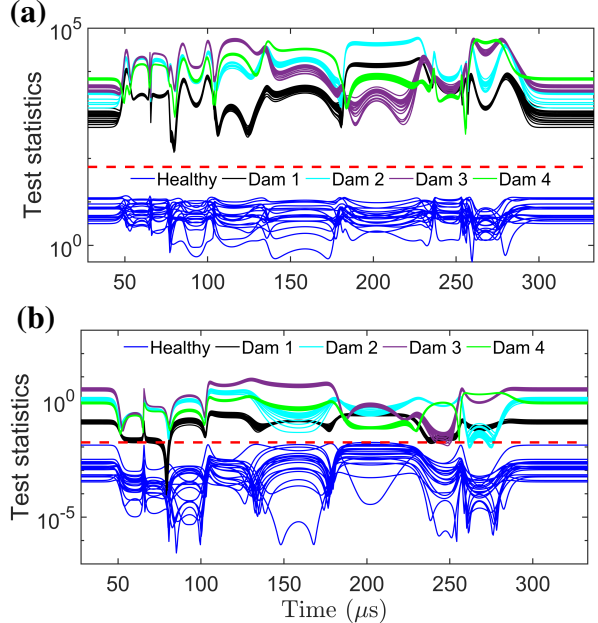


Fig. 10. Time-varying damage detection performance of the FS-TAR(4)_[5,3] model for the aluminum plate for damage non-intersecting path 2-4: (a) using the experimental covariance matrix derived from 20 healthy realizations; and (b) using the FS-TAR(4)_[5,3] model-based covariance matrix.

skin is wrapped over internal structure with moltoprene foam filling. Figure 12(a) shows the entire rotorcraft blade while Figure 12(b) shows the part of the blade where the PZT sen-

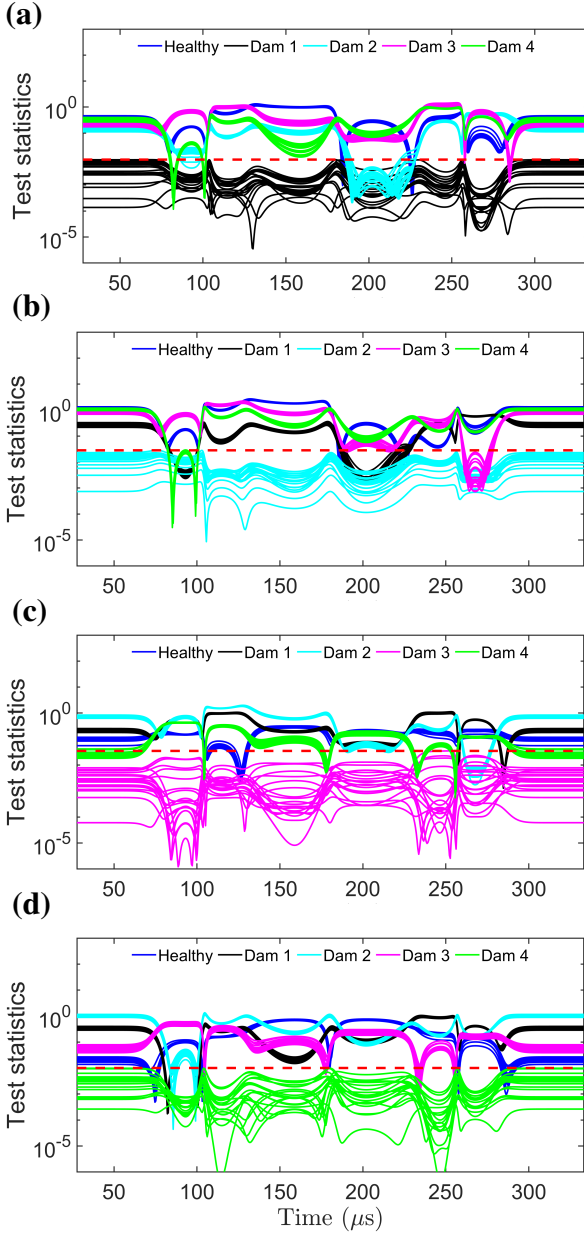


Fig. 11. Time-varying damage identification results for the aluminum plate for damage intersecting path 3-4 using the FS-TAR(4)_[4,2] model-based covariance matrix: (a) damage level 1; (b) damage level 2; (c) damage level 3; (d) damage level 4.

sors were mounted. Using Hysol EA 9394 adhesive, six lead zirconate titanate (PZT) piezoelectric sensors (type PZT-5A, Acellent Technologies, Inc) of 6.35 mm (1/4 in) diameter and a thickness of 0.2 mm (0.0079 in) were attached to the plate and cured for 24 hours in room temperature. The distance between the sensor pair (1,4), (2,5) and (3,6) is 6 inches. And the distance between the sensor pair (1,2), (2,3), (4,5) and (5,6) is 3 inches. Sensors 1 and 4 are 2.8 inches apart from the left edge. Similarly, sensors 3 and 6 are 2.8 inches apart from the right edge. Up to five three-gram weights were taped to the surface of the rotor blade starting from its center-point to simulate local damage as shown in Figure 12(b). Data acquisition

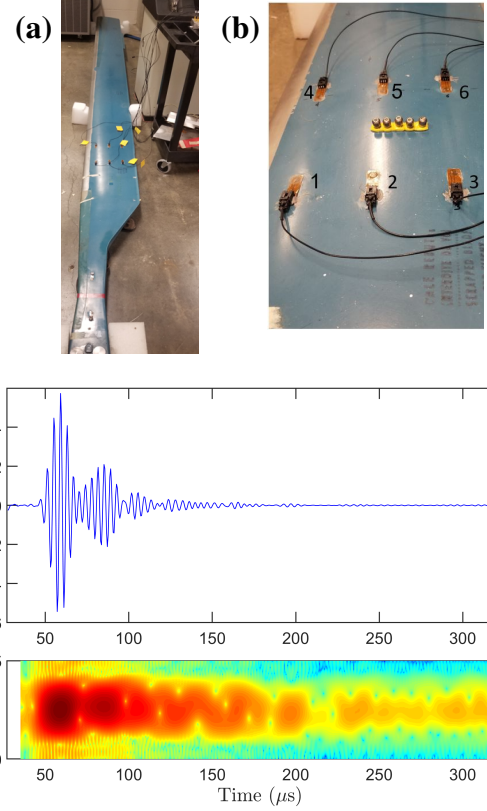


Fig. 12. Experimental setup and signal of the full-scale rotocraft blade: (a) full-scale rotocraft blade with sensors; (b) PZT sensors arrangement on the rotocraft blade; (c) indicative signal from the blade and the non-parametric spectrogram for path 1-4.

and analysis were done in the same manner as in the case of the aluminum coupon.

Figure 12(c) show a typical response signal from path 1-4 and its spectrogram. Note that unlike aluminum plate, the response signal dies out quickly after 150 μ s. This occurs due to the moltoprene foam filling which absorbs the signal due to its viscous nature. As a result, the length of the available signal for damage detection and identification of the rotocraft blade is shorter compared to the aluminum plate.

Parametric Identification and Damage Detection Results for the Helicopter Blade

Similar to the aluminum plate, for the case of the rotocraft blade, an integer optimization scheme was used for determining the basis indices. For path 3-4, the best model occurred for $na = 4$ and the functional subspaces are $\mathcal{F}_{AR} = \{G_1[t], G_3[t]\}$ ($pa = 2$) and $\mathcal{F}_{\sigma_e} = \{G_1[t], G_2[t]\}$ ($ps = 2$). This is compactly written as FS-TAR(4)_[2,2]. Similarly, for path 2-4, the best model occurred for $na = 2$ and $\mathcal{F}_{AR} = \{G_1[t]\}$ ($pa = 1$) and $\mathcal{F}_{\sigma_e} = \{G_1[t]\}$ ($ps = 1$) compactly written as FS-TAR(2)_[1,1]. Note that for damage non-intersecting path 2-4 only one basis function is used. As the index $ba = 1$, so it is basically a constant. This, in principle, reduces the FS-TAR model into an AR model, where the parameters are essentially constant.

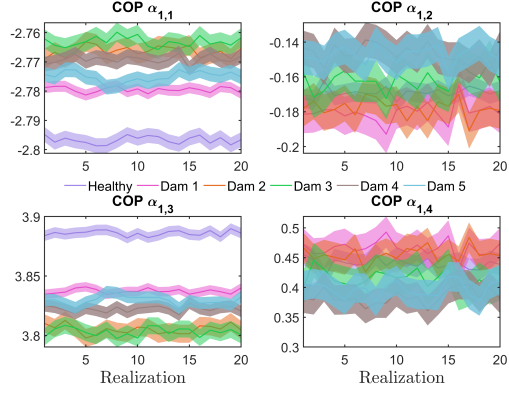


Fig. 13. Coefficients of projection (COP) for different structural states for the rotorcraft blade coupon for damage intersecting path 3-4 using the wavelet basis function: the COP mean is shown as solid lines and the associated ± 2 standard deviations as shaded regions.

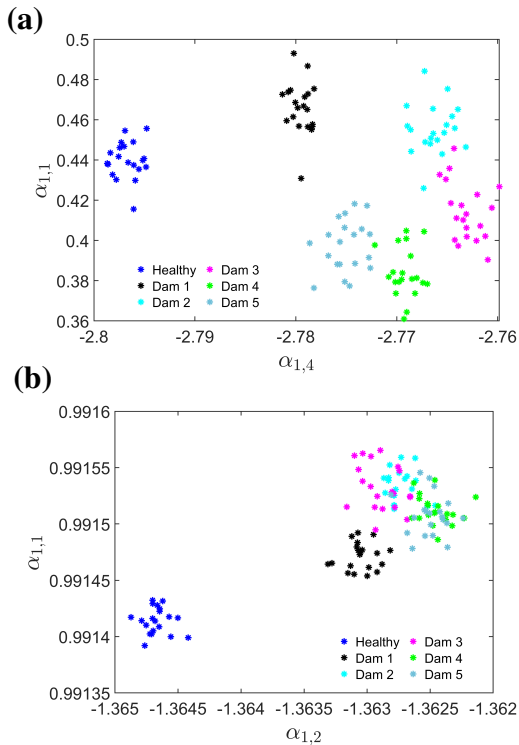


Fig. 14. Correlation between the coefficients of projection for different paths of the rotorcraft blade: (a) for damage intersecting path 3-4; and (b) for damage non-intersecting path 2-4 .

However, the FS-TAR(2)_[1,1] model is required for damage detection and identification for the damage non-intersecting path in the rotorcraft blade. Maximum-likelihood estimator was used again for estimating the coefficients of projection vector ϑ .

Figure 13 depict the first four AR coefficients of projection (COP) using the wavelet basis function for damage intersecting path 3-4 for all different structural states, namely: healthy, damage level 1, damage level 2, damage level 3,

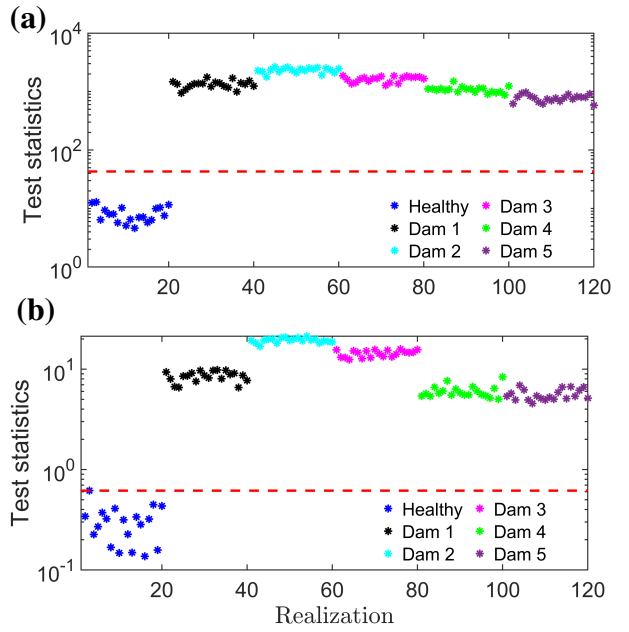


Fig. 15. Damage detection performance of the FS-TAR(4)_[2,2] model for the rotorcraft blade for damage intersecting path 3-4: (a) using the experimental covariance matrix derived from 20 healthy realizations; and (b) using the FS-TAR(4)_[2,2] model-based covariance matrix.

damage level 4 and damage level 5. For wavelet basis functions and damage intersecting path 3-4, there are 8 AR COP in total ($na \cdot pa = 4 \cdot 2 = 8$). Among these 8 (2 for damage non-intersecting path 2-4) AR COPs, the first four, namely: $\alpha_{1,1}, \alpha_{1,2}, \alpha_{1,3}, \alpha_{1,4}$ are shown. For each state, 20 realizations are shown. The solid lines represent the mean COP values, and the shaded regions represent the ± 2 experimental standard deviation confidence intervals. In Figure 13 (for damage intersecting path 3-4), for the COP $\alpha_{1,2}$ and $\alpha_{1,4}$, note that different damage states are overlapped on each other and the corresponding confidence intervals are relatively wider. On the other hand, for the COP $\alpha_{1,1}$ and $\alpha_{1,3}$, different damage states are partially overlapped and the corresponding confidence intervals are slightly narrower.

Figure 14(a) shows the correlation between the COP $\alpha_{1,1}$ and COP $\alpha_{1,4}$ for damage intersecting path 3-4. Note that different realizations of damage level 2 and 3 overlap on each other. In addition, the group formed by different realizations of damage level 2, 3, 4, and 5 remain close to each other. Only the healthy realizations and damage level 1 are well separated. Figure 14(b) shows the correlation between the COP $\alpha_{1,1}$ and COP $\alpha_{1,2}$ for damage non-intersecting path 2-4. Note that, in this case, all the realizations of damage level 1, 2, 3, 4, and 5 are overlapped on each other. Only the healthy realizations remain well separated.

Figure 15 shows the damage detection performance for the rotorcraft blade for damage intersecting path 3-4 using the wavelet basis functions. In Figure 15(a), the covariance matrix was derived from the 20 experimental healthy signals and in Figure 15(b), FS-TAR(4)_[2,2] model-based covariance ma-

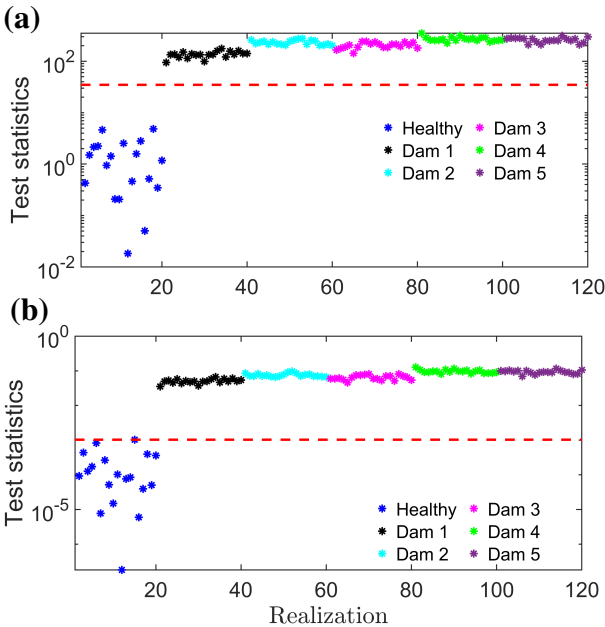


Fig. 16. Damage detection performance of the FS-TAR(2)_[1,1] model for the rotorcraft blade for damage non-intersecting path 2-4: (a) using the experimental covariance matrix derived from 20 healthy realizations; and (b) using the FS-TAR(2)_[1,1] model-based covariance matrix.

trix was used. Note that for both cases, perfect damage detection was achieved. The α level used in Figure 15(a) was 1×10^{-8} . In Figure 15(b), it was manually adjusted as α level gets close to 1. Similarly, Figure 16 shows the damage detection performance of the damage non-intersecting path 2-4. Note that perfect damage detection was achieved in this case too. The α level used in Figure 16(a) was 1×10^{-8} while it was manually adjusted in Figure 16(b).

Figure 17 shows the damage identification performance for the damage intersecting path 3-4 for the rotorcraft blade for different damage states using the experimental covariance matrix derived from 20 healthy realizations. Note that perfect damage identification was achieved with no missed classification. As for example, when identifying damage level 3 (Figure 17(c)), all the test statistics for damage level 3 remain below the threshold (dotted red line) and the test statistics for all other damage levels go outside the threshold. Healthy test statistics are also shown to reinforce the fact that simultaneous damage detection and identification are possible using the same identified model structure.

Figure 18 shows the time-varying damage detection using the wavelet basis function for damage intersecting path 3-4. In Figure 18(a), experimental covariance matrix derived from 20 experimental healthy signals and in Figure 18(b), FS-TAR(4)_[2,2] model-based covariance matrix were used. In this case, instead of using the constant COPs, four time-varying parameters (as the model order is $na = 4$) α_1 , α_2 , α_3 , and α_4 were used with the associated time-varying covariance. Note that the 20 healthy realizations of the time-varying test statistics (solid blue lines) lie below the threshold (dotted red

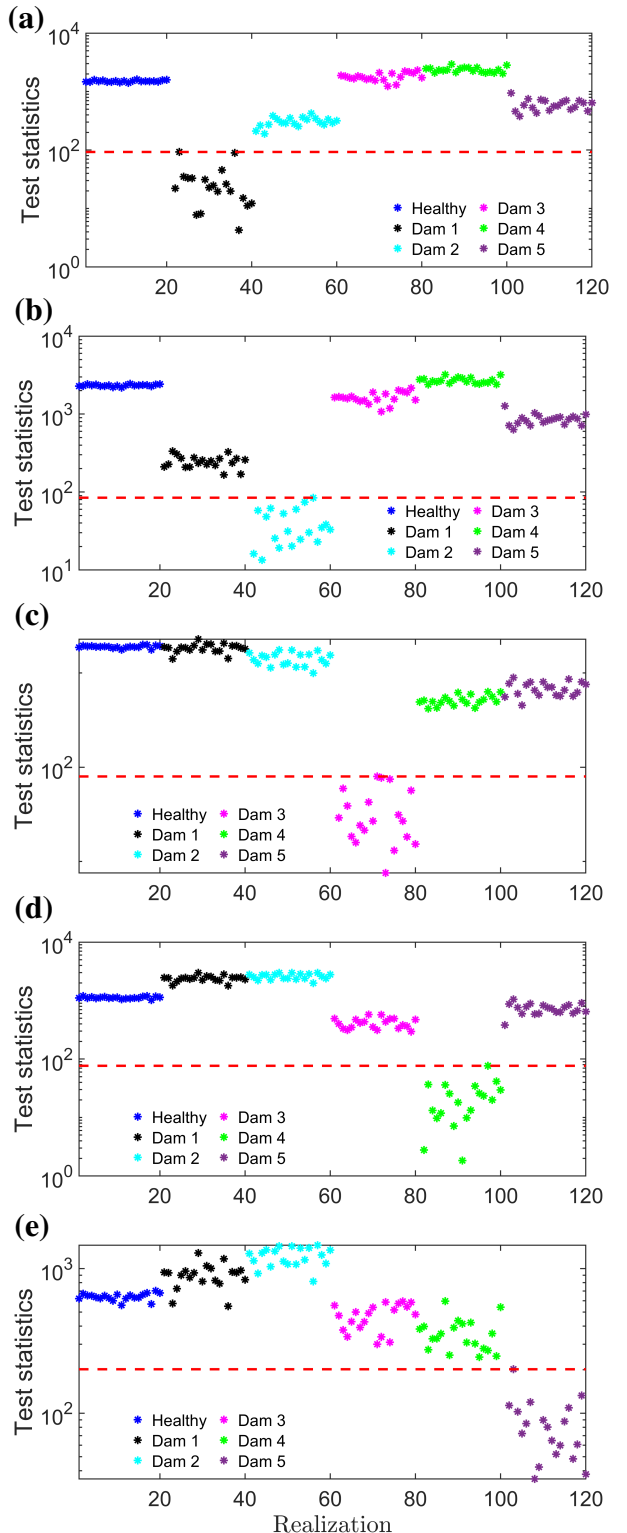


Fig. 17. Damage identification results of the FS-TAR(4)_[2,2] model for the rotorcraft blade for damage intersecting path 3-4 using the experimental covariance matrix derived from 20 healthy realizations: (a) damage level 1; (b) damage level 2; (c) damage level 3; (d) damage level 4; (e) damage level 5.

line) for all time instants. And the time-varying test statistics for damage level 1, 2, 3, 4, and 5 (all realizations) crosses the

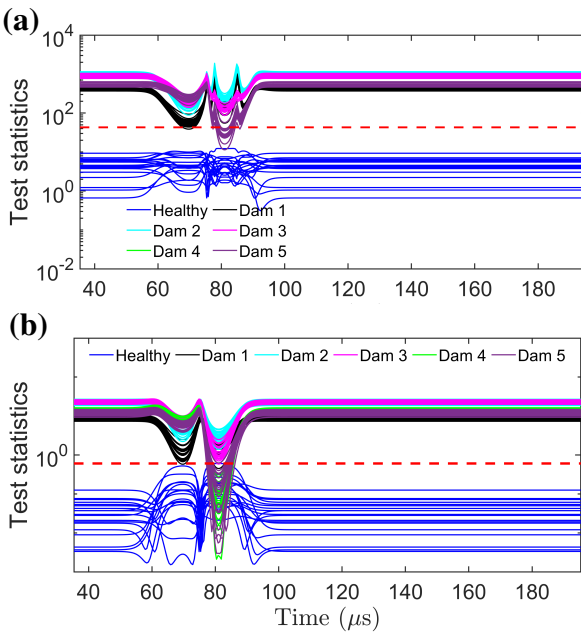


Fig. 18. Time-varying damage detection performance of the FS-TAR(4)_[2,2] model for the rotorcraft blade for damage intersecting path 3-4: (a) using the experimental covariance matrix derived from 20 healthy realizations; and (b) using the FS-TAR(4)_[2,2] model-based covariance matrix.

threshold. As a result, perfect damage detection was achieved for damage intersecting path using both the experimental and theoretical covariance matrix. The α level used in Figure 18(a) was 1×10^{-8} . On the other hand, it was manually adjusted for Figure 18(b).

Figure 19 shows the time-varying damage identification results for the rotorcraft blade for damage intersecting path 3-4. In this case, experimental covariance matrix derived from 20 healthy realizations was used. Note that perfect damage identification was achieved for all different damage levels. That is, the corresponding structural state lies below the threshold for all the time instants and all other structural states cross the threshold for at least at one time instant.

CONCLUDING REMARKS

The objective of this work was the experimental assessment of a statistical damage diagnosis framework in the context of ultrasonic guided wave-based damage diagnosis using parametric stochastic time-varying time series models on a full-scale rotorcraft blade. In the FS-TAR formulation, model parameters evolve in a deterministic way as they are projected onto appropriate functional subspaces. The model parameters were used to diagnose damage based on the definition of statistical quantities and corresponding hypothesis testing procedures.

Before presenting the damage diagnosis results on the rotorcraft blade, damage detection in an aluminum plate is discussed first. It was found that, for the aluminum plate, perfect damage detection and identification are possible both for damage intersecting and non-intersecting paths. The use of

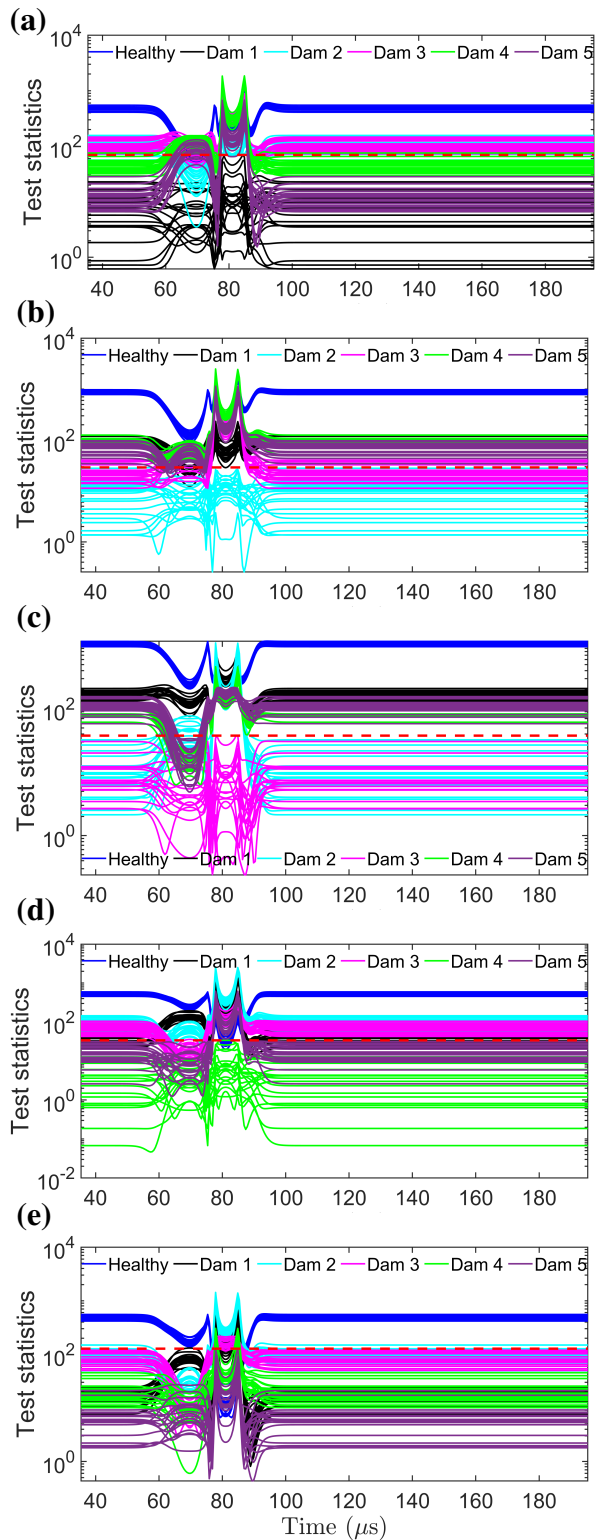


Fig. 19. Time-varying damage identification results of the FS-TAR(4)_[2,2] model for the rotorcraft blade for damage intersecting path 3-4 using the experimental covariance matrix derived from 20 healthy realizations: (a) damage level 1; (b) damage level 2; (c) damage level 3; (d) damage level 4; (e) damage level 5.

a specific type of covariance matrix, that is, either the experimental or the theoretical one does not change the outcome

of the damage diagnosis process. Again, from the aluminum plate, a longer signal is available as the signals do not die out so quickly as the rotorcraft blade.

Using the same approach as in the aluminum plate, perfect damage detection and identification for the rotorcraft blade were achieved only for the damage intersecting paths. For damage non-intersecting paths, perfect damage detection but partial damage identification was achieved. Again, for the case of the rotorcraft blade, the use of experimental covariance matrix results in perfect damage detection and identification. The theoretical covariance matrix was not used in this case, because it results in missed damage and damage misclassifications. Again, the signal length is relatively shorter as it dies out quickly due to the viscous nature of the foam core used in the construction of the composite rotorcraft blade. In conclusion, the results of this study indicated that ultrasonic waves modeled by the FS-TAR models can be used to perform health monitoring of rotorcraft blades.

ACKNOWLEDGMENTS

This work is carried out under the support of the U.S. Air Force Office of Scientific Research (AFOSR) grant “Formal Verification of Stochastic State Awareness for Dynamic Data-Driven Intelligent Aerospace Systems” (FA9550-19-1-0054) with Program Officer Dr. Erik Blasch.

REFERENCES

- ¹Schenck, E., Davis, M., Bond, R., Meyer, J., and Rusak, D., “Integrated Hybrid Structural Management System (IHSMS) – aircraft impact monitoring,” American Helicopter Society 73rd Annual Forum Proceedings, Fort Worth, Texas, May 2017.
- ²LeFevre, B., Davis, M., Marr, C., Rusak, D., and Johnson, C., “Integrated Hybrid Structural Management System (IHSMS): usage and loads monitoring,” American Helicopter Society 73st Annual Forum & Technology Display Proceedings, Fort Worth, Texas, May 2017.
- ³Ibáñez, F., Baltazar, A., and Mijarez, R., “Detection of damage in multiwire cables based on wavelet entropy evolution,” *Smart Materials and Structures*, Vol. 24, (8), 2015, pp. 085036.
- ⁴Su, Z., Zhou, C., Hong, M., Cheng, L., Wang, Q., and Qing, X., “Acousto-ultrasonics-based fatigue damage characterization: Linear versus nonlinear signal features,” *Mechanical Systems and Signal Processing*, Vol. 45, (1), 2014, pp. 225–239.
- ⁵Ahmed, S. and Kopsaftopoulos, F. P., “Uncertainty quantification of guided waves propagation for active sensing structural health monitoring,” Proceedings of the Vertical Flight Society 75th Annual Forum & Technology Display, May 2019.
- ⁶Qiu, L., Yuan, S., and Boller, C., “An adaptive guided wave-Gaussian mixture model for damage monitoring under time-varying conditions: Validation in a full-scale aircraft fatigue test,” *Structural health monitoring*, Vol. 16, (5), 2017, pp. 501–517.
- ⁷Haynes, C., Todd, M. D., Flynn, E., and Croxford, A., “Statistically-based damage detection in geometrically-complex structures using ultrasonic interrogation,” *Structural Health Monitoring*, Vol. 12, (2), 2013, pp. 141–152.
- ⁸Amer, A. and Kopsaftopoulos, F. P., “Statistical guided-waves-based structural health monitoring via stochastic non-parametric time series models,” *Structural Health Monitoring*, 2021, pp. 1–28.
- ⁹Fassois, S. D. and Kopsaftopoulos, F. P., “Statistical time series methods for vibration based structural health monitoring,” *New trends in structural health monitoring*, Springer, 2013, pp. 209–264.
- ¹⁰Kopsaftopoulos, F. P. and Fassois, S. D., “Vibration based health monitoring for a lightweight truss structure: experimental assessment of several statistical time series methods,” *Mechanical Systems and Signal Processing*, Vol. 24, 2010, pp. 1977–1997.
- ¹¹Ahmed, S. and Kopsaftopoulos, F., “Stochastic Identification of Guided Wave Propagation under Ambient Temperature via Non-Stationary Time Series Models,” *Sensors*, Vol. 21, (16), 2021.
doi: 10.3390/s21165672
- ¹²Roy, S., Lonkar, K., Janapati, V., and Chang, F.-K., “A novel physics-based temperature compensation model for structural health monitoring using ultrasonic guided waves,” *Structural Health Monitoring*, Vol. 13, (3), 2014, pp. 321–342.
- ¹³Poulimenos, A. and Fassois, S., “Parametric time-domain methods for non-stationary random vibration modelling and analysis—a critical survey and comparison,” *Mechanical systems and signal processing*, Vol. 20, (4), 2006, pp. 763–816.
- ¹⁴Spiridonakos, M. and Fassois, S., “An FS-TAR based method for vibration-response-based fault diagnosis in stochastic time-varying structures: experimental application to a pick-and-place mechanism,” *Mechanical Systems and Signal Processing*, Vol. 38, (1), 2013, pp. 206–222.
- ¹⁵Sotiriou, D., Kopsaftopoulos, F., and Fassois, S., “An adaptive time-series probabilistic framework for 4-D trajectory conformance monitoring,” *IEEE Transactions on Intelligent Transportation Systems*, Vol. 17, (6), 2016, pp. 1606–1616.
- ¹⁶Ljung, L., *System Identification: Theory for the User*, Prentice-Hall, second edition, 1999.
- ¹⁷Akaike, H., “Prediction and Entropy,” A Celebration of Statistics, edited by A. C. Atkinson and S. E. Fienberg, 1985.
- ¹⁸Schwarz, G., “Estimating the Dimension of a Model,” *The Annals of Statistics*, Vol. 6, (2), 1978, pp. 461 – 464.